ACS APPLIED MATERIALS & INTERFACES

www.acsami.org

Research Article

Mechanically Strong and Thermally Insulating Polyimide Aerogel Fibers Reinforced by Prefabricated Long Polyimide Fibers

Chenyu Zhu, Tiantian Xue, Zhuocheng Ma, Wei Fan,* and Tianxi Liu*

Cite This: *ACS Appl. Mater. Interfaces* 2023, 15, 12443−12452

Read Online

ACCESS | Metrics & More | Article Recommendations | Supporting Information

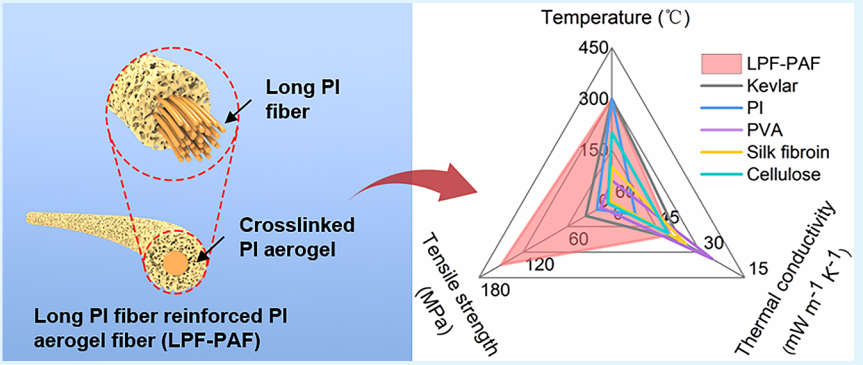

ABSTRACT: Aerogel fibers inherit the merits of aerogel and fibrous materials, such as high porosity and satisfactory knittability, demonstrating great potential as thermal protective materials applied in harsh environments. Nevertheless, the inferior mechanical property resulting from the porous structure immensely hampers the practical application of aerogel fibers. Herein, we develop robust and thermally insulating long polyimide fiber-reinforced polyimide composite aerogel fibers (LPF-PAFs). The porous crosslinked polyimide aerogel as the sheath endows LPF-PAFs with good thermal insulation performance, while the long polyimide fibers as the core provide LPF-PAFs with superior mechanical strength. Due to the introduction of the high-strength long polyimide fibers to undertake significant stress, LPF-PAFs display outstanding strength surpassing 150 MPa without obvious mechanical performance degeneration in a wide range of temperatures from −100 to 300 °C. Moreover, the textile woven by LPF-PAFs exhibits a superior thermal insulation ability and stability to cotton textile at 200 and −100 °C, indicating its potential application in thermal protective clothing under extreme environments.

KEYWORDS: *aerogel fiber, long fiber, polyimide, mechanical reinforcement, thermal insulation*

1. INTRODUCTION

Thermally insulating fibrous materials have long been used to protect humans from the damage of high temperature and chilliness and maintain a suitable human body temperature.[1−3] Because of their unique morphology, fibrous materials usually display outstanding thermal insulation effects and knittability to meet the requirements of diverse application conditions, which are widely applied in thermally insulating clothing.[4−7] To date, a series of thermally insulating fibrous materials have been exploited, including cellulose,[8,9] protein,[10,11] synthetic fibers,[12,13] etc. However, owing to their inferior heat resistance and unsatisfactory thermal insulation effect, these traditional fibrous materials are incapable of satisfying the need for thermal insulation in extreme conditions, such as aerospace, fire scene, and polar regions, which severely restricts the expansion of scientific research and the living environment.[14−16] Hence, for achieving thermal insulation on the human body under harsh environments, developing novel and efficient thermally insulating fibers is a matter of great urgency.

In recent years, aerogel fiber, one-dimensional aerogel material, inheriting the merits of aerogel materials, for instance, high porosity, large specific surface area, and low density, arouses wide interest in thermal insulation, electromagnetic shielding, and adsorption fields.[17−19] In particular, the thermal conductivity of aerogel fibers can be effectively limited because the porous structure restricts air convection, heat radiation, and thermal conduction.[20,21] Therefore, aerogel fiber is considered a promising candidate for thermally insulating clothing. Various aerogel fibers have been developed based on different raw materials and preparation techniques, including cellulose,[22] silk fibroin,[23] Kevlar,[24] polyimide,[25] etc. Among

Received: January 10, 2023
Accepted: February 13, 2023
Published: February 22, 2023

https://doi.org/10.1021/acsami.3c00408
ACS Appl. Mater. Interfaces 2023, 15, 12443−12452

them, polyimide aerogel fibers show superior mechanical performance and thermal insulation effects.[26] Due to the conjugated structure, polyimide aerogels have superior mechanical properties to many inorganic aerogels (silica, ceramic, etc.).[27] Moreover, polyimide aerogels' heat resistance is better than most organic aerogels, such as cellulose and protein.[28,29] Therefore, polyimide aerogels can be employed in high-temperature environments. Additionally, chemically crosslinked polyimide aerogels promote strength and reduce shrinkage.[30] Therefore, polyimide aerogel fiber has been demonstrated as a promising material for thermally insulating clothing.

Unfortunately, the highly porous structure of aerogel fibers also causes deterioration of their mechanical performance, which is a huge obstacle hindering the practical application of aerogel fibers.[31−33] Hence, great efforts have been devoted to improving the mechanical properties of aerogel fibers by researchers around the world. On the one hand, matrix material lays the groundwork for the final mechanical performance of fibers. As a result, Wang et al. prepared a polyimide aerogel fiber with oriented pores via freeze-spinning technology, and the strength was elevated to 12 MPa.[25] On the other hand, the spinning process is another important factor resulting in the distinction of mechanical properties of fibers. Recently, a universal method to prepare aerogel fibers with the help of rubber tubes was exploited by Zhang's group, and the obtained crosslinked polyimide aerogel fiber showed a high strength of 17 MPa and a low shrinking percentage.[34] However, the mechanical performance of aerogel fibers is still far from the standard of commercial fibers. It remains an immense challenge to design high-strength and thermally insulating aerogel fibers.

As we know, composite materials have the advantage of strong designability and excellent properties, which have been popular in industrial applications and scientific research over past decades.[35−37] Based on the composite reinforcement theories, fillers with various shapes have been developed to improve the mechanical properties of composite materials, including particles,[38] lamellae,[39] short fibers,[40] long fibers,[41] etc. It is worth noting that the addition of long fibers can more significantly improve the mechanical properties of the composites since the long fibers can undertake most of the stress. It can effectively protect composites from fracture and has been employed to strengthen composite materials through 3D printing technology. For example, He et al. compounded the resin matrix with long carbon fibers by a direct ink writing technique, which realized the construction of freestanding and high-strength composites exceeding 200 MPa along the fiber direction.[42] Hence, the long fiber is believed to exhibit promising potential in reinforcing soft and porous materials like foams, aerogels, etc.

Inspired by 3D printed long fiber reinforced composites, we have developed a robust and thermally insulating long polyimide fiber-reinforced polyimide aerogel fiber (LPF-PAF). The LPF-PAFs with the core−sheath structure are prepared by an injection method and a rubber tube-assisted molding process. The porous crosslinked polyimide aerogel as the sheath endows LPF-PAFs with good thermal insulation performance, while the long polyimide fibers as the core provide LPF-PAFs with superior mechanical strength. During stretching, long inner fibers bear most of the stress and limit the strain of the whole composite fiber, which can effectively protect the aerogel sheath from damage. At the same time, the core and sheath materials are both polyimides, which have good compatibility, ensuring that the aerogel layer is tightly wrapped on the long fibers. Therefore, LPF-PAFs exhibit outstanding tensile strength exceeding 150 MPa without obvious mechanical performance degeneration in a wide range of temperatures from −100 to 300 °C. Meanwhile, LPF-PAFs also display great stability of thermal insulation at 300 and −100 °C, showing their promising potential as thermal insulation material applied in extreme conditions.

2. EXPERIMENTAL SECTION

2.1. Materials. 3,3′,4,4′-Biphenyltetracarboxylic dianhydride (BPDA, 99%), 2,2′-dimethylbenzidine (DMBZ, 98%), 1,3,5-tris(4-aminophenyloxy)benzene (TAB, 98%), 1-methyl-2-pyrrolidinone (NMP, 99%), acetic anhydride (99%), pyridine (98%), and ethanol (99.5%) were purchased from Sinopharm Chemical Reagent Co., Ltd. A long polyimide fiber (LPF) bundle was bought from Jiangsu Aoshen New Material Co., Ltd. The LPF bundle with a diameter of ∼100 μm was made of single polyimide fibers with a diameter of ∼20 μm. Silicone rubber tubes (inside diameter of 500 μm, outside diameter of 2 mm) were obtained from Guangdong Shengpai Insulation Material Co., Ltd.

2.2. Preparation of Precursor Solution. A polyamic acid (PAA) oligomer was first prepared from polycondensation of BPDA and DMBZ. First, x mol (x = 0.01) of DMBZ was thoroughly dissolved in NMP under vigorous stirring. Moreover, the amount of NMP was controlled in light of the solid content of obtained PAA solution. Then, y mol of BPDA was slowly added into the solution under stirring according to the required polymerization degree (n), which could be calculated based on the following equation:

$$\frac{y}{x} = \frac{n+1}{n} \tag{1}$$

After stirring for 4 h, z mol of TAB as a crosslinker was mixed with the solution by stirring for another 30 min. The additive amount of TAB could be calculated according to eq 2:

$$z = \frac{2}{3}(y - x) \tag{2}$$

After that, 8.0 mL of acetic anhydride (97%) and 4.0 mL of pyridine (99%) were introduced into the PAA solution successively, and the mixed precursor solution should be immediately used in the following injection process.

2.3. Preparation of Long Polyimide Fiber-Reinforced Polyimide Aerogel Fiber (LPF-PAF). Polyimide composite aerogel fiber was fabricated with the assistance of rubber tubes. In the first step, prefabricated LPF bundles with a diameter of 100 μm were threaded into rubber tubes with an inner diameter of 500 μm. Then, the above fresh prepared precursor solution was transferred into a syringe and injected into the tube until the tube was full. To keep the LPF bundle in the center of the rubber tube as possible, additional rings (outside diameter of ∼500 μm, inside diameter of ∼200 μm) were installed at both ends of the rubber tubes, and LPF bundles were threaded into rings and tightened (schematically shown in Figure S1). Due to the continuous occurrence of chemical imidization reactions, PAA gradually transformed into crosslinked polyimide, and the gel skeleton was gradually formed. After standing for 12 h, the gelation process was complete. Subsequently, the gel fibers were separated from tubes with ethanol (99%) and repeatedly washed in ethanol to remove residual NMP. Finally, LPF-PAFs were prepared by supercritical CO_2 drying, getting rid of the ethanol in gel fibers with a gas pressure of 10 MPa at 50 °C.

In order to explore the effect of the solid content of the aerogel on LPF-PAFs, the precursor PAA solutions with different solid contents (2.5, 5.0, 7.5, and 10.0 wt %) were prepared. As an example, LPF-PAF preparation from PAA with a solid content of 7.5 wt % and n = 35 is described as follows: 2.120 g of DMBZ was thoroughly dissolved in 63.440 g of NMP, and 3.024 g of BPDA was slowly added into the

https://doi.org/10.1021/acsami.3c00408
ACS Appl. Mater. Interfaces 2023, 15, 12443−12452

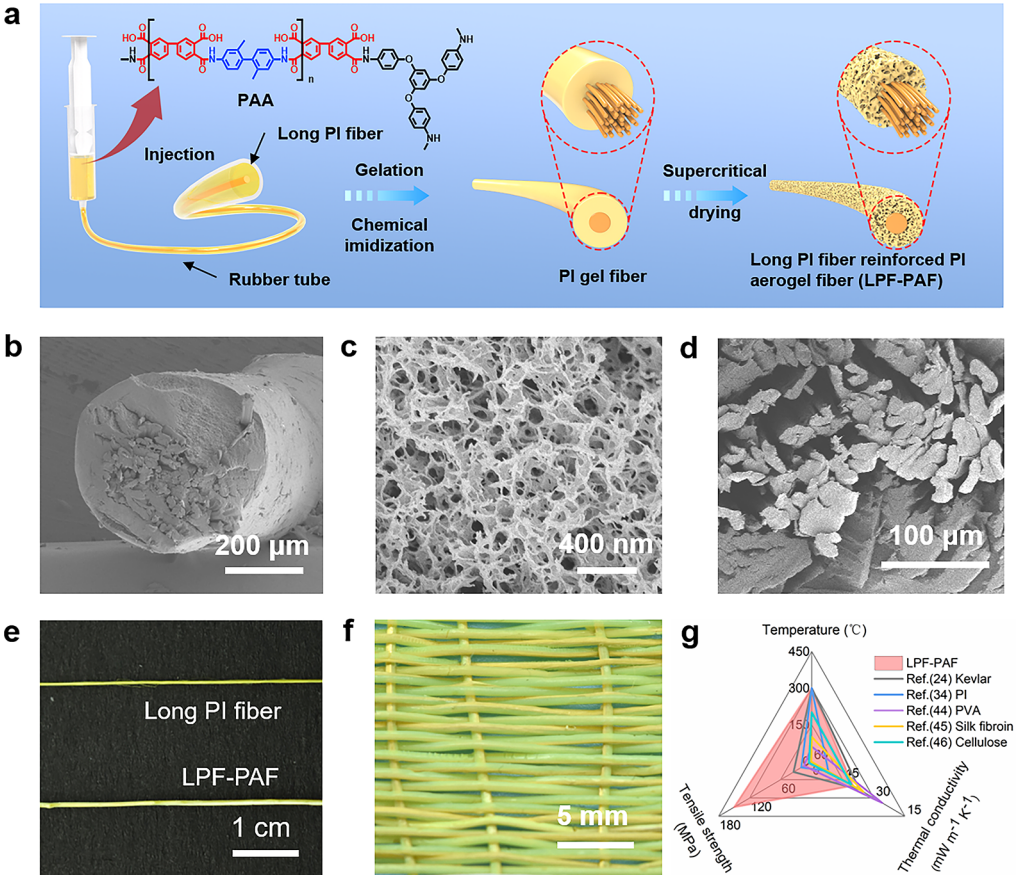

Figure 1. Preparation and morphology of LPF-PAFs with a core−sheath structure. (a) Schematic diagram of fabrication of LPF-PAFs. (b) Cross-sectional SEM image of LPF-PAF. (c) Cross-sectional SEM image of aerogel sheath showing a porous structure. (d) Cross-sectional morphology of a solid polyimide fiber core (LPF bundle, 100 μm). (e) Photographs of a single LPF-PAF and an LPF bundle. (f) Exhibition of fabric woven with LPF-PAFs. (g) Comparison of the heat resistance performance, thermal insulation capability, and mechanical property between LPF-PAF and other aerogel fibers reported in the literature.

solution under stirring. After stirring for 4 h, 0.076 g of TAB was mixed with the solution by stirring for another 30 min. After that, 8.0 mL of acetic anhydride and 4.0 mL of pyridine were introduced successively to get the mixed precursor solution for the following injection process. The LPF-PAFs were fabricated through the same injection process mentioned above. The obtained LPF-PAFs prepared from PAA solutions with different solid contents were labeled as LPF-PAF *S*, where *S* means the solid content.

2.4. Material Characterizations. Scanning electron microscopy (SEM, JSM-7500F, Japan) was applied to record the cross-sectional morphology and the aerogel structure of LPF-PAFs. To test the specific surface area and pore size distribution of samples, Brunauer−Emmett−Teller (BET) and Barrett−Joyner−Halenda (BJH) methods (Autosorb iQ2, Quantachrome instrument, USA) were adopted. The chemical structure of crosslinked polyimide was analyzed by Fourier transform infrared spectroscopy (FTIR, Nicolet8700, USA). In addition, the thermal stability of diverse aerogels was characterized by a thermogravimetric analyzer (TGA, TA Q5000IR, Germany) under a nitrogen atmosphere (10 K min^{-1}). Dynamic mechanical analysis (DMA, TA-Q800, USA) testing was carried out in the frequency sweep mode with fixed temperatures (−100, 25, and 300 °C) and strain (0.3%). The infrared images were taken by a thermal infrared camera (FOTRIC 226s, Fluke, USA). The hydrophobicity of LPF-PAFs was displayed by applying a dynamic contact angle testing instrument (OSA200, Germany). The mechanical performance of the composite aerogel fiber was tested by a tensile testing machine (UTM2102, Suns, China) with a gauge length of 50 mm and an extension speed of 10 mm min^{-1}. As shown in Video S1, the aerogel fibers were held vertically with a fixture and stretched along the fiber until it broke. The thermal conductivity of composite aerogel fiber was measured by a Hot Disk TPS 2500 S instrument (Hot Disk AB, Sweden). As shown in Figure S2, LPF-PAFs were arranged parallelly into a fiber felt (length × width × height: 4 cm × 4 cm × 5 mm), and the ends of fibers were taped. Moreover, the Kapton probe (diameter of 21 mm, type 7854, Hot Disk AB, Sweden) was placed in the middle of the fiber felt (half the height of the fiber felt) to measure the thermal conductivity. The shrinkage and porosity were calculated according to eqs 3 and 4 as follows:

$$S = \left(1 - \frac{V}{V_0}\right) \times 100\% \tag{3}$$

$$P = \left(1 - \frac{\rho}{\rho_S}\right) \times 100\% \tag{4}$$

where *S* and *P* are the shrinkage and porosity of LPF-PAFs, respectively, *V* stands for the actual volume of samples, V_0 signifies the volume of samples before drying, ρ represents the apparent density, while ρ_s means the skeletal density of samples (ρ_s = 1.4 g cm^{-3}).[43] To ensure the reliability of the data, each datum was collected from at least five samples.

3. RESULTS AND DISCUSSION

3.1. Preparation and Characterization of LPF-PAFs. The whole preparation process of LPF-PAFs is clearly illustrated in Figure 1a. In this process, the crosslinked polyimide (PI) was obtained by chemical imidization of synthesized PAA solution crosslinked with TAB (Figure S3).

https://doi.org/10.1021/acsami.3c00408
ACS Appl. Mater. Interfaces 2023, 15, 12443−12452

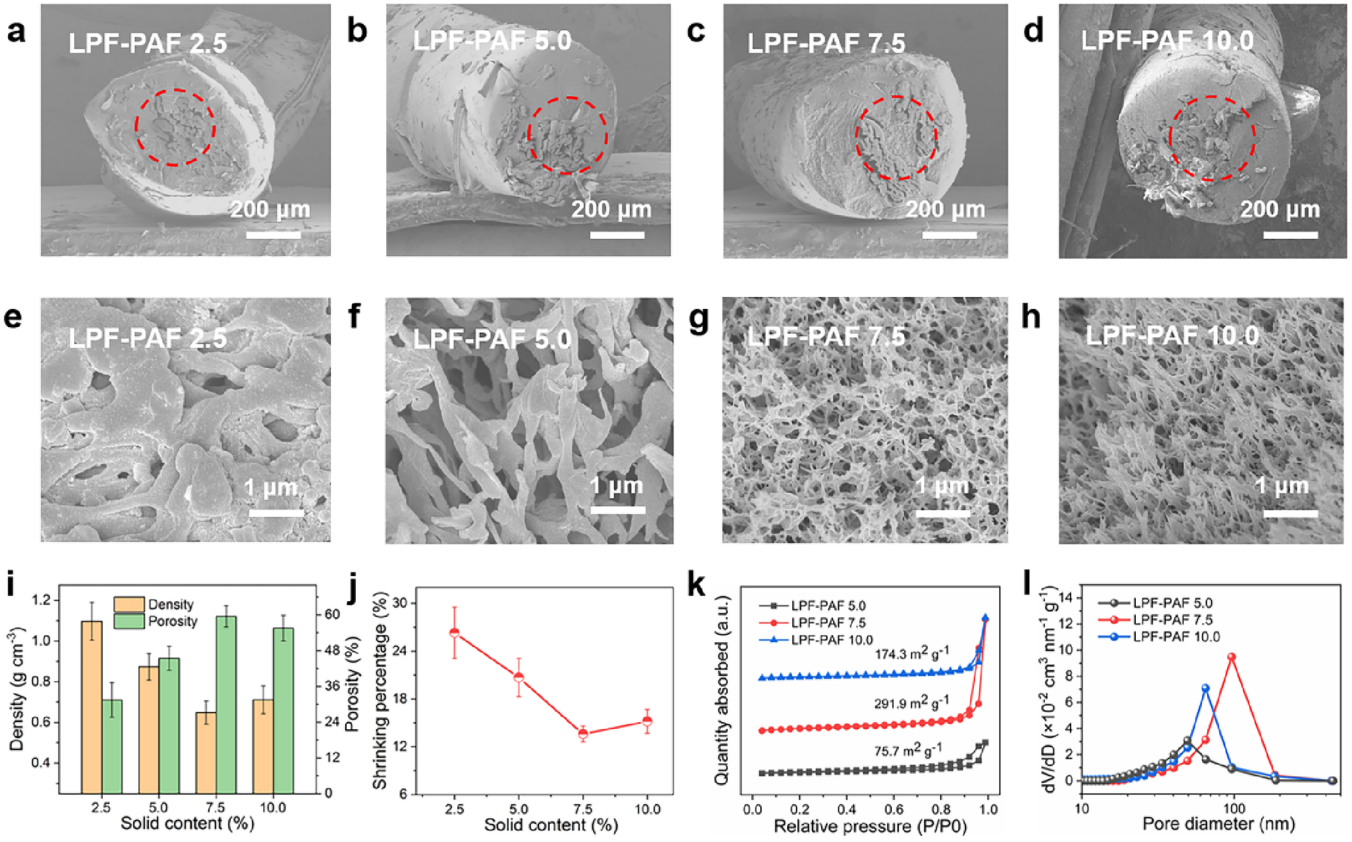

Figure 2. Porous structure and morphology of LPF-PAFs. (a–d) Cross-sectional SEM images of LPF-PAF-containing aerogels with varying solid contents (S = 2.5, 5.0, 7.5, and 10.0 wt %). The red circle indicates the LPF bundle. (e–h) Porous structure of the crosslinked polyimide aerogel of LPF-PAFs. (i) Porosity and density and (j) shrinking percentage of LPF-PAFs. (k) N_2 adsorption–desorption isotherms and (l) pore size distribution of the aerogel sheath of LPF-PAFs.

First, the PAA precursor solution was injected into the rubber tube containing LPF to get the polyimide composite gel fiber by a chemical imidization reaction. Subsequently, after gelation, solvent replacement, and supercritical CO_2 drying in sequence, the crosslinked polyimide gel was turned into an aerogel, and LPF-PAFs with the core–sheath structure were obtained. In this core–sheath structure, the crosslinked polyimide aerogel with low shrinkage was employed as the sheath to improve the thermal insulation behavior. In contrast, the LPF bundle was employed as a core to bear most of the stress and enhance the mechanical strength of the whole composite fiber. In addition, the core and sheath are both polyimides, enabling good compatibility between the aerogel sheath and the LPF bundle, which can further improve the mechanical strength. Therefore, the prepared LPF-PAF has outstanding mechanical properties and retains great thermal insulation and heat resistance.

As intuitively displayed in Figure 1b, LPF-PAF shows a core–sheath structure with a loose aerogel sheath and a dense core, demonstrating the successful combination of the polyimide aerogel and the LPF bundle. In more detail, the diameter of LPF-PAF is around 450 μm according to the cross-sectional SEM image, a bit smaller than the inner diameter of the rubber tube (500 μm), which is due to the shrinkage of the aerogel during gelation and the supercritical drying process. The enlarged SEM image of the aerogel sheath is exhibited in Figure 1c, and a mass of nanopores of about 100 nm could be observed, demonstrating the typical porous morphology of the aerogel. In addition, compared with the morphology of neat polyimide aerogel fiber (PAF) (Figure S4a,b), the introduction of an LPF bundle has no obvious effect on the porous structure of the aerogel. The core of LPF-PAFs consists of an LPF bundle containing single fibers with a diameter of 20 μm (Figure 1d), which can offer a larger interface area to interact with the aerogel sheath, benefiting the mechanical performance of LPF-PAFs. There is no evident difference between the original LPF bundle (Figure S4c) and the LPF in the composite fiber, indicating the structural stability of the LPF bundle during processing and the feasibility of this reinforcement method. In addition, the LPF bundle is still in the center of LPF-PAF after the preparation process, avoiding the LPF bundle separating from composite fibers during use (Figure S5). In Figure 1e, LPF-PAF shows a pale-yellow appearance with a larger diameter than the yellow LPF bundle, owing to the aerogel sheath. More importantly, the resulting composite aerogel fibers still have a certain degree of flexibility that can be bent and weaved (Figure S6). As shown in Figure 1f, LPF-PAFs could be weaved into a 4 × 4 cm^2 aerogel fabric due to their good flexibility, proving their potential as thermally insulating clothing. Owing to the high porosity of the aerogel and reinforcement of the LPF bundle as well as the good thermal stability of polyimide, LPF-PAFs have great advantages in heat resistance (300 °C), thermal insulation (0.040 W m^{-1} K^{-1} at room temperature), and mechanical strength (150 MPa), which is superior to previously reported aerogel fibers (Figure 1g).[24,34,44−46]

3.2. Regulation of the Aerogel Structure of LPF-PAFs.

The porosity and structure of the aerogel sheath greatly

https://doi.org/10.1021/acsami.3c00408
ACS Appl. Mater. Interfaces 2023, 15, 12443−12452

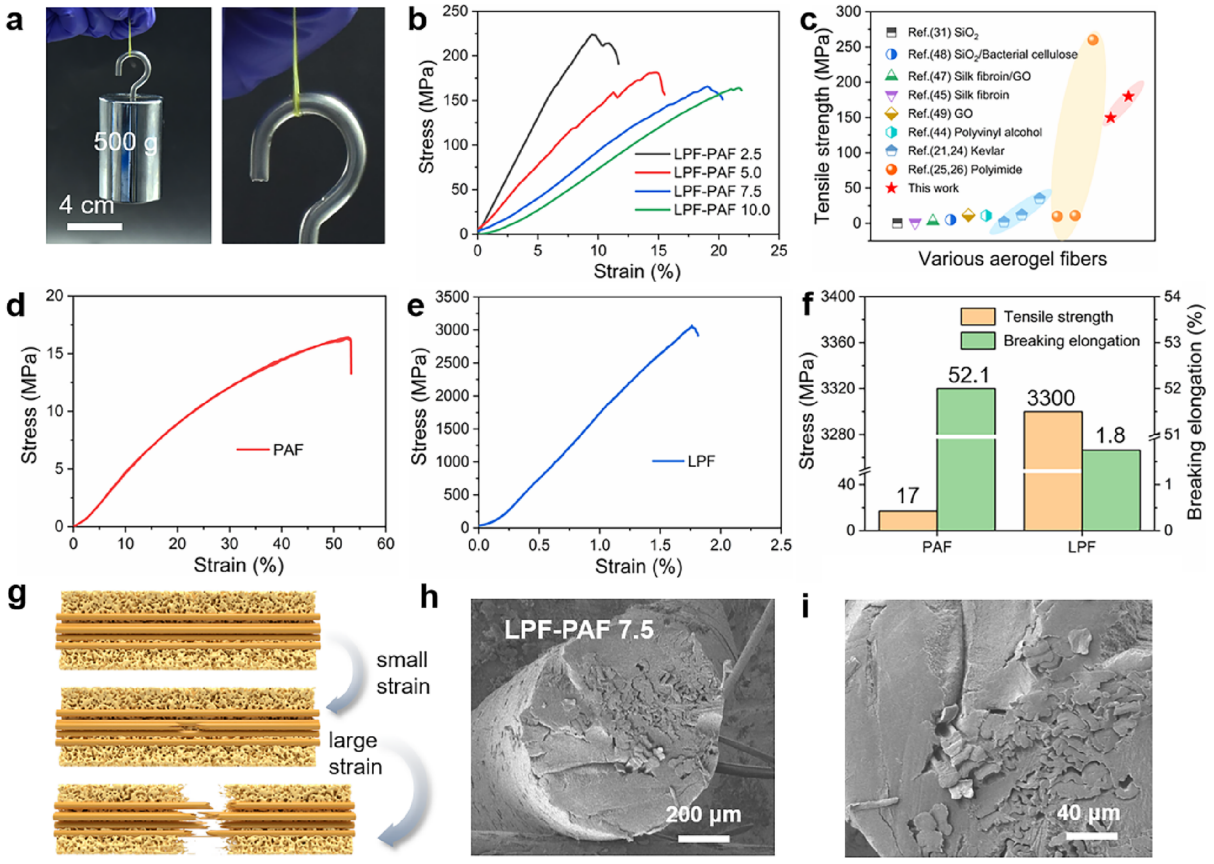

Figure 3. Mechanical performance of LPF-PAFs. (a) Single LPF-PAF 7.5 could stand a 500 g weight without breaking. (b) Mechanical performance of LPF-PAFs with diverse solid contents of crosslinked polyimide. (c) Comparison of mechanical performance between LPF-PAFs and other aerogel fibers reported in the literature. Tensile stress−strain curve of (d) neat PAF and (e) neat LPF. (f) Tensile strength and breaking elongation of PAF and LPF. (g) Proposed tensile fracture mechanism. The yellow part signifies the aerogel, and the orange part is LPF. (h,i) Cross-sectional SEM images of LPF-PAF 7.5 at different magnifications.

influence the mechanical and thermal insulation performance of LPF-PAFs. To optimize the porosity and density of the aerogel sheath, two crucial parameters, namely, the solid content (S) and the polymerization degree (n) of crosslinked polyimide, are studied in detail. As manifested in Figure S7, FTIR spectra of crosslinked polyimide aerogels with various polymerization degrees (n = 20, 35, 50, and 65) represent similar characteristic peaks at 736, 1009, 1363, 1714, and 1776 cm^{-1}, which are ascribed to the imide bonds of polyimide, demonstrating the successful transformation of polyamic acid into polyimide.[34] To further verify the crosslinking process, we tested the thermal stability of crosslinked polyimide aerogels in a nitrogen atmosphere. With the increment of the polymerization degree, the decomposition temperatures (T_{d5} and T_{dmax}) of aerogels gradually decrease according to the TGA curves shown in Figure S8, which is due to the decrease of the crosslinking density. The porous structure of the LPF-PAF-containing aerogel with different polymerization degrees shows no discernible difference, as observed by SEM images in Figure S9. The density, porosity, and shrinkage of corresponding LPF-PAFs exhibit only small fluctuations with different polymerization degrees (Figure S10), of which the sample (n = 35) has the lowest density of 0.65 g cm^{-3}, a cortex shrinkage of 13.3%, and the largest specific surface area of 291.9 m^2 g^{-1}. Therefore, unless specifically mentioned, LPF-PAF (n = 35) is selected for further discussion.

In addition, we also investigated the impact of the solid content of crosslinked polyimide on the porous structure of the aerogel sheath. When the solid content of the PAA precursor solution increases from 2.5 to 5.0, 7.5, and 10.0 wt %, the cross-sectional area of LPF-PAFs first rises and then falls and reaches the maximum at 7.5 wt %, according to the SEM images in Figure 2a−d. In fact, this phenomenon could be explained by the variation of the porous structure of the aerogel sheath in Figure 2e−h. At low solid contents of 2.5 and 5 wt %, the skeleton of the crosslinked polyimide aerogel markedly shrinks and even thoroughly collapses (Figure 2e,f). The porous structure of the aerogel is preserved when the solid content exceeds 7.5 wt %, and the pore size is restricted to ∼100 nm (Figure 2g,h). Correspondingly, the LPF-PAF 7.5 exhibits the optimal density and porosity with the lowest shrinkage of the aerogel sheath (Figure 2i,j). We also tested the aerogel sheath's specific surface area and pore size distribution with different solid contents. The LPF-PAF 7.5 exhibits the largest specific surface area of 291.9 m^2 g^{-1}, compared to 174.3 and 75.7 m^2 g^{-1} of LPF-PAF 10.0 and LPF-PAF 5.0, respectively (Figure 2k). In addition, the specific surface area of LPF-PAF 7.5 is a bit smaller than that of neat PAF (317.2 m^2 g^{-1}), which may be caused by the introduction of the solid LPF bundle (Figure S11). It could be seen that the peak of the pore size distribution of the LPF-PAF 7.5 aerogel layer is around 100 nm, which is in accordance with the SEM image (Figure 2l). The deviation of the pore size distribution of LPF-

https://doi.org/10.1021/acsami.3c00408
ACS Appl. Mater. Interfaces 2023, 15, 12443−12452

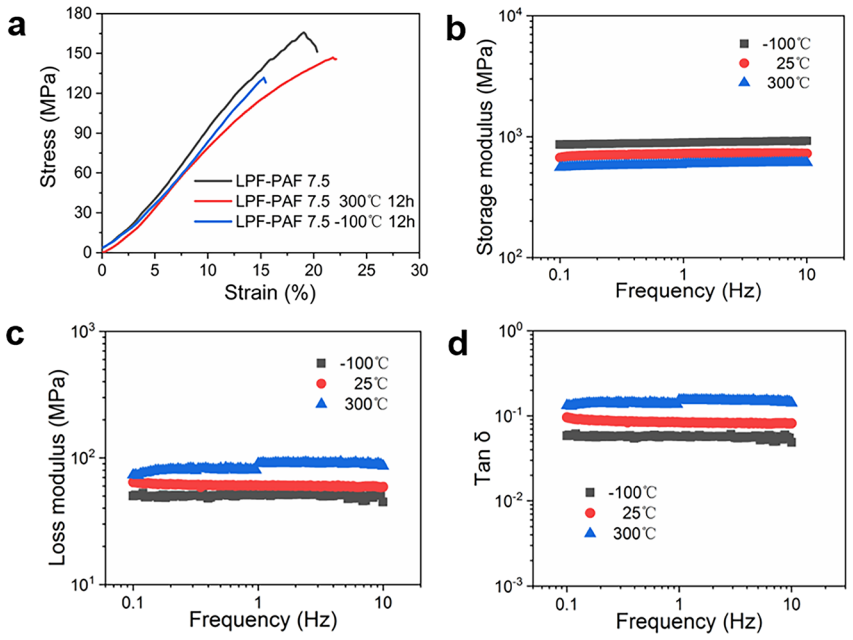

Figure 4. Mechanical stability of LPF-PAFs under various temperatures. (a) Stress−strain curves of LPF-PAF 7.5 under various conditions (treated at room temperature, 300 °C, and −100 °C for 12 h). (b−d) Storage modulus, loss modulus, and loss factor (tan δ) of LPF-PAF 7.5 at distinct temperatures measured by DMA, demonstrating its superior structural stability under harsh environments.

PAF 10.0 and LPF-PAF 5.0 may result from nonspherical pores owing to the shrinkage.

3.3. Mechanical Properties of LPF-PAFs. The mechanical performance of LPF-PAFs with the core−sheath structure was evaluated. The photographs in Figure 3a show that a single LPF-PAF 7.5 could hold up to a 500 g weight without breaking, demonstrating its robust mechanical property. The influence of the aerogel sheath on the mechanical performance of LPF-PAFs was further investigated. When the solid content of crosslinked polyimide gradually increases from 2.5 to 10.0 wt %, the strength of corresponding LPF-PAFs displays a gradual decline while the breaking elongation increases ceaselessly (Figure 3b). Due to the higher porosity, wider diameter, and larger cross-sectional area of LPF-PAF 7.5 and LPF-PAF 10.0, the strength of around 150 MPa is lower than those of LPF-PAF 2.5 (223 MPa) and LPF-PAF 5.0 (178 MPa). The breaking elongations of LPF-PAF 7.5 (19%) and LPF-PAF 10.0 (21%) are elevated compared to those of LPF-PAF 2.5 (9%) and LPF-PAF 5.0 (15%). It is the result of the good elongation ability of the loose aerogel layer. According to the integral area under the tensile curves in Figure 3b, the toughness of LPF-PAF 7.5 can be calculated as 18.1 MJ m^{-3}, which is higher than those of LPF-PAF 2.5 (16.1 MJ m^{-3}), LPF-PAF 5.0 (16.7 MJ m^{-3}), and LPF-PAF 10.0 (17.9 MJ m^{-3}). In addition, it seems that the polymerization degree of the aerogel sheath has little effect on the mechanical property of LPF-PAFs, as illustrated in Figure S12. Therefore, considering both strength and toughness, LPF-PAF 7.5 was chosen for further study. Compared with other aerogel fibers in the literature, the obtained LPF-PAFs (150 MPa) are stronger than most, indicating this reinforcement method's rationality (Figure 3c).[21,24−26,31,44,45,47−49] As shown by stress−strain curves in Figure 3d,e, neat PAF displays a low tensile strength of 17 MPa, which is far lower than that of LPF, indicating the significance of LPF for enhancing the strength of LPF-PAF. According to the classical composite reinforcement theory, the strength of composites consisting of a soft matrix and long fibers is controlled by five parameters, namely, the ultimate strength of the matrix (X_m) and long fibers (X_f), the ultimate strain of long fibers (ε), the strength of the matrix at an ultimate strain of long fibers (X_ε), and the volume fraction of long fibers (C_f). According to Figure 3f, these parameters could be found (X_m = 17 MPa, X_f = 3300 MPa, ε = 1.8%, and X_ε = 2 MPa). Due to the known diameters of the LPF bundle (100 μm) and LPF-PAFs (500 μm), C_f could be calculated as 0.04 according to the ratio of the cross-sectional area of the LPF bundle and LPF-PAFs. Based on the theory, there is one crucial volume fraction parameter (C_r) calculated according to the following equation (eq 5).[50,51]

$$C_r = \frac{X_m - X_\varepsilon}{X_f - X_\varepsilon} \tag{5}$$

when C_f surpasses C_r, it means that composites break after breaking long fibers and the long fibers undertake the major stress. In this work, C_f (0.04) outclasses C_r (0.0045). Hence, we propose the fracture mechanism of LPF-PAFs as illustrated in Figure 3g. The yellow part signifies the aerogel, and the orange part is the long fiber. When LPF-PAFs are stretched exceeding ε, the long fibers will fracture gradually, accompanied by the slippage between the aerogel sheath and long fibers. Owing to the good compatibility between long fibers and the aerogel sheath, long fibers are tightly wrapped by the aerogel sheath (Figure 3h,i). Friction between them also helps to improve the strength, increasing the elongation and delaying the fracture of LPF-PAFs. With the accumulation of slippages and small strains, LPF-PAFs finally break at a certain stretching, and the aerogel sheath breaks at the same time. Therefore, LPF-PAFs exhibit a high strength and toughness of 150 MPa and 18.1 MJ m^{-3}, respectively, resulting from the high strength of long fibers and the good compatibility between long fibers and the aerogel sheath.

The mechanical performance of LPF-PAFs over a wide temperature range of −100 to 300 °C in air was further

https://doi.org/10.1021/acsami.3c00408
ACS Appl. Mater. Interfaces 2023, 15, 12443−12452

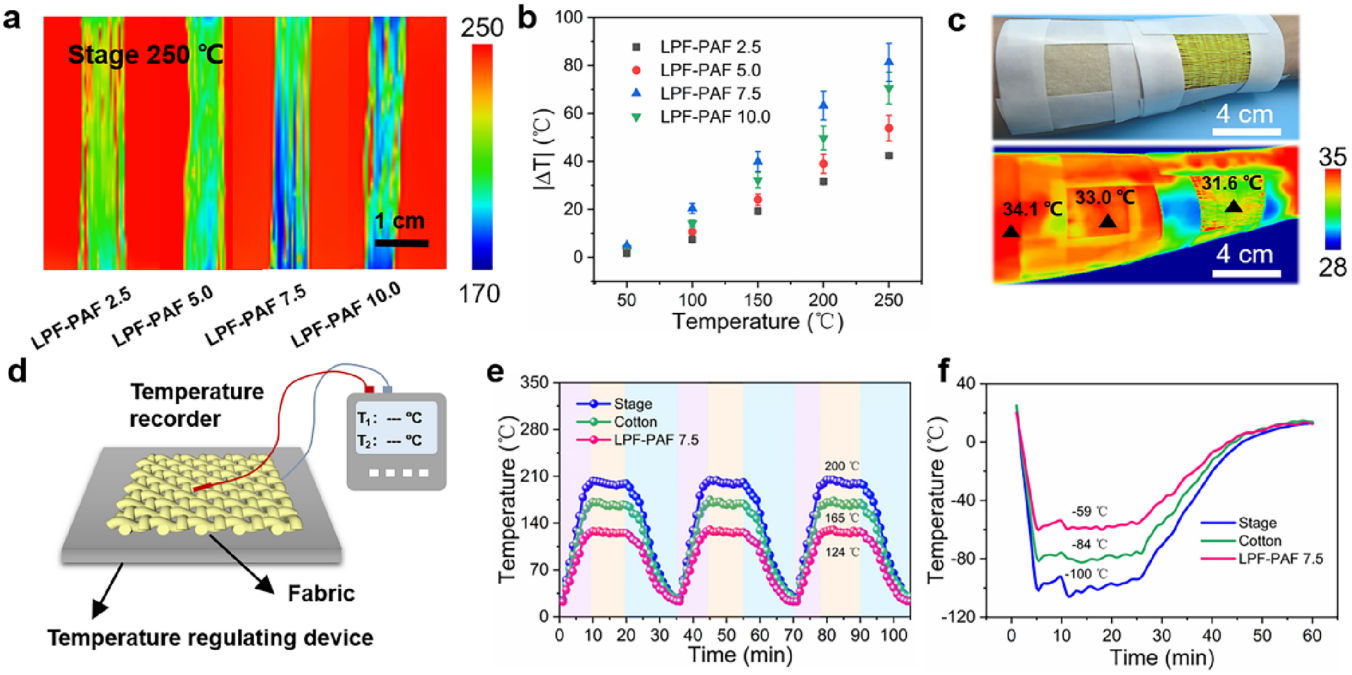

Figure 5. Thermal insulation property of LPF-PAF and its textile. (a) Infrared thermal image of LPF-PAF bundles (800 μm thickness) on a 250 °C platform. (b) Temperature difference ($|\Delta T|$) between the fiber surface and the measuring platform plotted against the platform temperature. (c) Comparison of the thermal insulation effect of LPF-PAF textile and cotton textile with the identical thickness (500 μm) and size (4 × 4 cm^2) on the human arm by an infrared thermal image. (d) Schematic diagram of the testing device for thermal insulation. (e,f) Temperature−time curves of the surface of LPF-PAF textile and cotton textile with stage temperature changing.

evaluated. After being exposed to 300 and −100 °C environments for 12 h, the mechanical strength of LPF-PAF 7.5 remains unchanged (around 150 MPa), illustrating the outstanding temperature resistance and superior structural stability of LPF-PAFs (Figure 4a). To further confirm the temperature-invariant mechanical properties, the DMA test is carried out in the frequency sweep mode with fixed temperatures (−100, 25, and 300 °C). With the temperature increment from −100 to 300 °C, there is no significant change in the storage modulus and loss modulus. The loss factor remains around 0.1, indicating that the composite fiber has good temperature resistance and structural stability (Figure 4b−d).

3.4. Thermal Insulation Performance of LPF-PAFs. The thermal insulation effect of LPF-PAFs and textiles was measured by an infrared thermal imager. For the test, single LPF-PAF fibers were parallelly closely packed into arrays with the same thickness (800 μm) and width (6 mm) on a hot stage, and infrared thermal images were recorded by a thermal imager above the hot stage. Figure 5a displays the infrared thermal images of LPF-PAF 2.5, LPF-PAF 5.0, LPF-PAF 7.5, and LPF-PAF 10.0 on the hot stage at 250 °C. From the infrared images, it is clearly indicated that LPF-PAF 7.5 has better thermal insulation behavior and owns the highest temperature difference ($|\Delta T|$ = 80 °C) between the surface of LPF-PAFs and the hot stage. That is due to the slow heat conduction and limited thermal convection originating from the high porosity and small pore size of LPF-PAF 7.5. Moreover, the thermal conductivities at room temperature of neat PAF, neat LPF, and LPF-PAF 7.5 are 36.7, 113.4, and 40.1 mW m^{-1} K^{-1}, respectively (Figure S13). Obviously, the thermal insulation performance of LPF-PAF is derived from the porous structure of the aerogel sheath, and the solid LPF core does not significantly influence thermal conductivity. We also detected the thermal insulation performance of LPF-PAFs at various temperatures. It could be concluded from Figure 5b that LPF-PAF 7.5 displays the highest temperature difference at a wide temperature range, demonstrating better thermal insulation properties under various temperatures. Subsequently, the practical thermal insulation effect of textile woven by LPF-PAF 7.5 is compared with commercial cotton textiles with an identical thickness (500 μm) and size (4 × 4 cm^2). The detailed weaving process is listed in Figure S14. Figure 5c shows that skin, cotton textile, and LPF-PAF textile surface temperatures are 34.1, 33.0, and 31.6 °C, respectively. The $|\Delta T|$ between the surface of LPF-PAF textile and the skin is 2.5 °C. In contrast, the $|\Delta T|$ between the commercial cotton fabric and the skin is only 1.1 °C, demonstrating the superior thermal insulation performance of LPF-PAFs. In addition, we also investigated the stability of thermal insulation of the obtained textile by a self-designed device, as indicated in Figure 5d. The thermocouples recorded the surface temperature of the textile and temperature regulating device. As illustrated in Figure 5e,f, the surface temperatures of the LPF-PAF textile are recorded as 124 and −59 °C after being tested on the temperature regulating platform of 200 and −100 °C, and those of cotton fabric are 165 and −84 °C. LPF-PAF textile has higher $|\Delta T|$ of 76 and 41 °C at 200 and −100 °C, respectively, compared to those of cotton textile of 35 and 16 °C. Moreover, LPF-PAF textile keeps a stable surface temperature when the platform is repeatedly heated to 200 °C for several cycles. These results suggest the superior thermal insulation ability and stability of LPF-PAFs. In addition, LPF-PAFs and the corresponding textile represent good hydrophobicity with no evident change of the water contact angle after being heated at 200 °C for 12 h (Figure S15), demonstrating their good hydrophobicity and structure

https://doi.org/10.1021/acsami.3c00408
ACS Appl. Mater. Interfaces 2023, 15, 12443−12452

stability, which might be conducive to cleaning and avoiding pore blockage or shrinkage of LPF-PAFs.

4. CONCLUSIONS

In summary, we have fabricated a high-strength and thermally insulating long polyimide fiber-reinforced polyimide aerogel fiber (LPF-PAF). The long polyimide fibers and the cross-linked polyimide aerogel are successfully combined by injection and rubber tube molding to prepare the composite fiber with a core−sheath structure. On account of the high-strength long polyimide fibers undertaking major stress, the obtained LPF-PAFs show outstanding mechanical strength surpassing 150 MPa without obvious mechanical performance degeneration in a wide range of temperatures from −100 to 300 °C. Moreover, LPF-PAF 7.5 shows a high toughness of 18.1 MJ m^{-3} because of the high-strength long polyimide fibers and the loose aerogel sheath. In addition, the low shrinkage and the porous polyimide aerogel sheath endow LPF-PAFs with satisfactory thermal insulation performance. The textile woven by LPF-PAFs could produce a $|\Delta T|$ of 2.5 °C between the surface of the textile and the skin, much larger than that of commercial cotton textile (1.1 °C) with identical thickness and size, demonstrating the outstanding thermal insulation ability of LPF-PAFs. Furthermore, the LPF-PAF textile exhibits superior thermal insulation stability to cotton textile at 200 and −100 °C, illustrating its potential for thermal insulation in extreme environments.

■ ASSOCIATED CONTENT

Supporting Information

The Supporting Information is available free of charge at https://pubs.acs.org/doi/10.1021/acsami.3c00408.

Schematic diagram of the fixing device of LPF; schematic diagram of the thermal conductivity test; synthetic route of crosslinked polyimide; SEM images of neat PAF and LPF; SEM image of LPF-PAF from the side; photograph of curving LPF-PAF; infrared spectra of crosslinked polyimide aerogels with distinct polymerization degrees; TGA curves of crosslinked polyimide aerogels with distinct polymerization degrees; cross-sectional SEM images of LPF-PAFs with distinct polymerization degrees; comprehensive performance of LPF-PAFs; N_2 adsorption−desorption isotherms of PAF; tensile test curves of LPF-PAFs with distinct polymerization degrees; thermal conductivity of PAF, LPF, and LPF-PAF; schematic diagram of the manual weaving device; hydrophobic property of LPF-PAF (PDF)

Aerogel fibers held vertically with a fixture and stretched along the fiber until its breakage (MP4)

■ AUTHOR INFORMATION

Corresponding Authors

Wei Fan − *State Key Laboratory for Modification of Chemical Fibers and Polymer Materials, College of Materials Science and Engineering, Donghua University, Shanghai 201620, China; Key Laboratory of Synthetic and Biological Colloids, Ministry of Education, School of Chemical and Materials Engineering, Jiangnan University, Wuxi 214122, China;* orcid.org/0000-0001-6978-1405; Email: weifan@dhu.edu.cn, weifan@jiangnan.edu.cn

Tianxi Liu − *State Key Laboratory for Modification of Chemical Fibers and Polymer Materials, College of Materials Science and Engineering, Donghua University, Shanghai 201620, China; Key Laboratory of Synthetic and Biological Colloids, Ministry of Education, School of Chemical and Materials Engineering, Jiangnan University, Wuxi 214122, China*; Email: txliu@jiangnan.edu.cn

Authors

Chenyu Zhu − *State Key Laboratory for Modification of Chemical Fibers and Polymer Materials, College of Materials Science and Engineering, Donghua University, Shanghai 201620, China*

Tiantian Xue − *State Key Laboratory for Modification of Chemical Fibers and Polymer Materials, College of Materials Science and Engineering, Donghua University, Shanghai 201620, China*

Zhuocheng Ma − *State Key Laboratory for Modification of Chemical Fibers and Polymer Materials, College of Materials Science and Engineering, Donghua University, Shanghai 201620, China*

Complete contact information is available at: https://pubs.acs.org/10.1021/acsami.3c00408

Author Contributions

C.Z. worked on the experiments, investigation, and data analysis and prepared the original draft. T.X. carried out the methodologies and data curation. Z.M. contributed to data curation and validation. W.F. contributed to conceptualization, methodology supervision, and review and editing of the manuscript. T.L. performed conceptualization, review and editing of the manuscript, and project administration.

Notes

The authors declare no competing financial interest.

■ ACKNOWLEDGMENTS

This work was supported by the National Natural Science Foundation of China (52073053 and 52233006), the Young Elite Scientists Sponsorship Program by CAST (2021QNRC001), the Shanghai Rising-Star Program (21QA1400300), the Innovation Program of Shanghai Municipal Education Commission (2021-01-07-00-03-E00108), the Science and Technology Commission of Shanghai Municipality (20520741100), and the China Postdoctoral Science Foundation (2021M690596).

■ REFERENCES

(1) Fisher, C. H. History of Natural Fibers. *J. Macromol. Sci., Part A: Pure Appl.Chem.* **1981**, *15*, 1345−1375.

(2) Stanković, S. B.; Popović, D.; Poparić, G. B. Thermal Properties of Textile Fabrics Made of Natural and Regenerated Cellulose Fibers. *Polym. Test.* **2008**, *27*, 41−48.

(3) Chen, Y. S.; Fan, J.; Zhang, W. Clothing Thermal Insulation During Sweating. *Text. Res. J.* **2003**, *73*, 152−157.

(4) Kaufman, W. C.; Bothe, D.; Meyer, S. D. Thermal Insulating Capabilities of Outdoor Clothing Materials. *Science* **1982**, *215*, 690−691.

(5) Hao, L.; Yu, W. Comparison of Thermal Protective Performance of Aluminized Fabrics of Basalt fiber and Glass fiber. *Fire Mater.* **2010**, *35*, 553−560.

(6) Mandal, S.; Mazumder, N.-U.-S.; Agnew, R. J.; Song, G.; Li, R. Characterization and Modeling of Thermal Protective and Thermo-Physiological Comfort Performance of Polymeric Textile Materials—A Review. *Materials* **2021**, *14*, 2397.

(7) Fu, M.; Weng, W. G.; Yuan, H. Y. Quantitative Assessment of the Relationship between Radiant Heat Exposure and Protective Performance of Multilayer Thermal Protective Clothing during Dry and Wet Conditions. *J. Hazard. Mater.* **2014**, *276*, 383−392.
(8) Tu, H.; Zhu, M.; Duan, B.; Zhang, L. Recent Progress in High-Strength and Robust Regenerated Cellulose Materials. *Adv. Mater.* **2021**, *33*, 2000682.
(9) Majumdar, A.; Mukhopadhyay, S.; Yadav, R. Thermal Properties of Knitted Fabrics Made from Cotton and Regenerated Bamboo Cellulosic Fibres. *Int. J. Therm. Sci.* **2010**, *49*, 2042−2048.
(10) Akcagun, E.; Bogus, M.; Hes, L. Thermal Insulation and Thermal Contact Properties of Wool and Wool/PES Fabrics in Wet State. *J. Nat. Fibers* **2019**, *16*, 199−208.
(11) Allafi, F.; Hossain, M. S.; Lalung, J.; Shaah, M.; Salehabadi, A.; Ahmad, M.; Shadi, A. Advancements in Applications of Natural Wool Fiber: Review. *J. Nat. Fibers* **2022**, *19*, 497−512.
(12) Wang, H.; Wang, P.; Zhang, Y.; Hu, D. Preparation and Characterization of Triangular Hollow Porous Polyacrylonitrile Fiber Made by Coaxial Wet Spinning. *J. Appl. Polym. Sci.* **2021**, *138*, 50816.
(13) Park, J. H.; Rutledge, G. C. 50th Anniversary Perspective: Advanced Polymer Fibers: High Performance and Ultrafine. *Macromolecules* **2017**, *50*, 5627−5642.
(14) Paul, H. L.; Diller, K. R. Comparison of Thermal Insulation Performance of Fibrous Materials for the Advanced Space Suit. *J. Biomech. Eng.* **2003**, *125*, 639−647.
(15) Yu, Z.; Liu, J.; Suryawanshi, A.; He, H.; Wang, Y.; Zhao, Y. Thermal Insulating and Fire-retarding Behavior of Treated Cotton Fabrics with A Novel High Water-retaining Hydrogel Used in Thermal Protective Clothing. *Cellulose* **2021**, *28*, 2581−2597.
(16) Kundu, C. K.; Song, L.; Hu, Y. Sol-gel Coatings from DOPO-Alkoxysilanes: Efficacy in Fire Protection of Polyamide 66 Textiles. *Eur. Polym. J.* **2020**, *125*, No. 109483.
(17) Tafreshi, O. A.; Mosanenzadeh, S. G.; Karamikamkar, S.; Saadatnia, Z.; Park, C. B.; Naguib, H. E. A Review on Multifunctional Aerogel Fibers: Processing, Fabrication, Functionalization, and Applications. *Mater. Today Chem.* **2022**, *23*, No. 100736.
(18) Liu, Z.; Lyu, J.; Ding, Y.; Bao, Y.; Sheng, Z.; Shi, N.; Zhang, X. Nanoscale Kevlar Liquid Crystal Aerogel Fibers. *ACS Nano* **2022**, *16*, 15237−15248.
(19) Li, M.; Chen, X.; Li, X.; Dong, J.; Zhao, X.; Zhang, Q. Controllable Strong and Ultralight Aramid Nanofiber-Based Aerogel Fibers for Thermal Insulation Applications. *Adv. Fiber Mater.* **2022**, *4*, 1267−1277.
(20) Xue, T.; Zhu, C.; Feng, X.; Wali, Q.; Fan, W.; Liu, T. Polyimide Aerogel Fibers with Controllable Porous Microstructure for Super-Thermal Insulation under Extreme Environments. *Adv. Fiber Mater.* **2022**, *4*, 1118−1128.
(21) Bao, Y.; Lyu, J.; Liu, Z.; Ding, Y.; Zhang, X. Bending Stiffness-Directed Fabricating of Kevlar Aerogel-Confined Organic Phase-Change Fibers. *ACS Nano* **2021**, *15*, 15180−15190.
(22) Li, Q.; Yuan, Z.; Zhang, C.; Hu, S.; Chen, Z.; Wu, Y.; Chen, P.; Qi, H.; Ye, D. Tough, Highly Oriented, Super Thermal Insulating Regenerated All-Cellulose Sponge-Aerogel Fibers Integrating A Graded Aligned Nanostructure. *Nano Lett.* **2022**, *22*, 3516−3524.
(23) Yang, H.; Wang, Z.; Liu, Z.; Cheng, H.; Li, C. Continuous, Strong, Porous Silk Firoin-Based Aerogel Fibers toward Textile Thermal Insulation. *Polymer* **2019**, *11*, 1899.
(24) Liu, Z.; Lyu, J.; Fang, D.; Zhang, X. Nanofibrous Kevlar Aerogel Threads for Thermal Insulation in Harsh Environments. *ACS Nano* **2019**, *13*, 5703−5711.
(25) Wang, Y.; Cui, Y.; Shao, Z.; Gao, W.; Fan, W.; Liu, T.; Bai, H. Multifunctional Polyimide Aerogel Textile Inspired by Polar Bear Hair for Thermoregulation in Extreme Environments. *Chem. Eng. J.* **2020**, *390*, No. 124623.
(26) Li, M.; Gan, F.; Dong, J.; Fang, Y.; Zhao, X.; Zhang, Q. Facile Preparation of Continuous and Porous Polyimide Aerogel Fibers for Multifunctional Applications. *ACS Appl. Mater. Interfaces* **2021**, *13*, 10416−10427.
(27) Shi, B.; Ma, B.; Wang, C.; He, H.; Qu, L.; Xu, B.; Chen, Y. Fabrication and Applications of Polyimide Nano-Aerogels. *Composites, Part A* **2021**, *143*, No. 106283.
(28) Ghaffari-Mosanenzadeh, S.; Tafreshi, O. A.; Karamikamkar, S.; Saadatnia, Z.; Rad, E.; Meysami, M.; Naguib, H. E. Recent Advances in Tailoring and Improving the Properties of Polyimide Aerogels and Their Application. *Adv. Colloid Interface Sci.* **2022**, *304*, No. 102646.
(29) Tafreshi, O. A.; Ghaffari-Mosanenzadeh, S.; Karamikamkar, S.; Saadatnia, Z.; Kiddell, S.; Park, C. B.; Naguib, H. E. Novel, flexible, and transparent thin film polyimide aerogels with enhanced thermal insulation and high service temperature. *J. Mater. Chem. C* **2022**, *10*, 5088−5108.
(30) Zheng, S.; Jiang, L.; Chang, F.; Zhang, C.; Ma, N.; Liu, X. Mechanically Strong and Thermally Stable Chemical Cross-Linked Polyimide Aerogels for Thermal Insulator. *ACS Appl. Mater. Interfaces* **2022**, *14*, 50129−50141.
(31) Du, Y.; Zhang, X.; Wang, J.; Liu, Z.; Zhang, K.; Ji, X.; You, Y.; Zhang, X. Reaction-Spun Transparent Silica Aerogel Fibers. *ACS Nano* **2020**, *14*, 11919−11928.
(32) Li, Y.; Zhang, X. Electrically Conductive, Optically Responsive, and Highly Orientated $Ti_3C_2T_x$ MXene Aerogel Fibers. *Adv. Funct. Mater.* **2021**, *32*, 2107767.
(33) He, H.; Liu, J.; Wang, Y.; Zhao, Y.; Qin, Y.; Zhu, Z.; Yu, Z.; Wang, J. An Ultralight Self-Powered Fire Alarm e-Textile Based on Conductive Aerogel Fiber with Repeatable Temperature Monitoring Performance Used in Firefighting Clothing. *ACS Nano* **2022**, *16*, 2953−2967.
(34) Li, X.; Dong, G.; Liu, Z.; Zhang, X. Polyimide Aerogel Fibers with Superior Flame Resistance, Strength, Hydrophobicity, and Flexibility Made via A Universal Sol-Gel Confined Transition Strategy. *ACS Nano* **2021**, *15*, 4759−4768.
(35) Park, S.; Shou, W.; Makatura, L.; Matusik, W.; Fu, K. 3D Printing of Polymer Composites: Materials, Processes, and Applications. *Matter* **2022**, *5*, 43−76.
(36) Hassani, S.; Mousavi, M.; Gandomi, A. H. Structural Health Monitoring in Composite Structures: A Comprehensive Review. *Sensors* **2022**, *22*, 153.
(37) Xiao, J.; Han, N.; Li, Y.; Zhang, Z.; Shah, S. P. Review of Recent Developments in Cement Composites Reinforced with Fibers and Nanomaterials. *Front. Struct. Civ. Eng.* **2021**, *15*, 1−19.
(38) Thankachan, T.; Prakash, K. S.; Kavimani, V. Investigating the Effects of Hybrid Reinforcement Particles on the Microstructural, Mechanical and Tribological Properties of Friction Stir Processed Copper Surface Composites. *Composites, Part B* **2019**, *174*, No. 107057.
(39) Xue, T.; Fan, W.; Zhang, X.; Zhao, X.; Yang, F.; Liu, T. Layered Double Hydroxide/Graphene Oxide Synergistically Enhanced Polyimide Aerogels for Thermal Insulation and Fire-retardancy. *Composites, Part B* **2021**, *219*, No. 108963.
(40) Avanzini, A.; Donzella, G.; Gallina, D.; Pandini, S.; Petrogalli, C. Fatigue Behavior and Cyclic Damage of Peek Short Fiber Reinforced Composites. *Composites, Part B* **2013**, *45*, 397−406.
(41) Kabir, S. M. F.; Mathur, K.; Seyam, A.-F. M. A Critical Review on 3D Printed Continuous Fiber-Reinforced Composites: History, Mechanism, Materials and Properties. *Compos. Struct.* **2020**, *232*, No. 111476.
(42) He, X.; Ding, Y.; Lei, Z.; Welch, S.; Zhang, W.; Dunn, M.; Yu, K. 3D Printing of Continuous Fiber-Reinforced Thermoset Composites. *Addit. Manuf.* **2021**, *40*, No. 101921.
(43) Pantoja, M.; Boynton, N.; Cavicchi, K. A.; Dosa, B.; Cashman, J. L.; Meador, M. A. B. Increased Flexibility in Polyimide Aerogels Using Aliphatic Spacers in the Polymer Backbone. *ACS Appl. Mater. Interfaces* **2019**, *11*, 9425−9437.
(44) Liu, Y.; Zhang, Y.; Xiong, X.; Ge, P.; Wu, J.; Sun, J.; Wang, J.; Zhuo, Q.; Qin, C.; Dai, L. Strategies for Preparing Continuous Ultraflexible and Ultrastrong Poly(Vinyl Alcohol) Aerogel Fibers with Excellent Thermal Insulation. *Macromol. Mater. Eng.* **2021**, *306*, 2100399.

https://doi.org/10.1021/acsami.3c00408
ACS Appl. Mater. Interfaces 2023, 15, 12443−12452

(45) Cui, Y.; Gong, H.; Wang, Y.; Li, D.; Bai, H. A Thermally Insulating Textile Inspired by Polar Bear Hair. *Adv. Mater.* **2018**, *30*, 1706807.
(46) Zhou, J.; Hsieh, Y.-L. Nanocellulose Aerogel-based Porous Coaxial Fibers for Thermal Insulation. *Nano Energy* **2020**, *68*, 104305.
(47) Wang, Z.; Yang, H.; Li, Y.; Zheng, X. Robust Silk Fibroin/Graphene Oxide Aerogel Fiber for Radiative Heating Textiles. *ACS Appl. Mater. Interfaces* **2020**, *12*, 15726−15736.
(48) Song, Q.; Miao, C.; Sai, H.; Gu, J.; Wang, M.; Jiang, P.; Wang, Y.; Fu, R.; Wang, Y. Silica-Bacterial Cellulose Composite Aerogel Fibers with Excellent Mechanical Properties from Sodium Silicate Precursor. *Gels* **2022**, *8*, 17.
(49) Xu, Z.; Zhang, Y.; Li, P.; Gao, C. Strong, Conductive, Lightweight, Neat Graphene Aerogel Fibers with Aligned Pores. *ACS Nano* **2012**, *6*, 7103−7113.
(50) Espinach, F. X.; Granda, L. A.; Tarrés, Q.; Duran, J.; Fullana-i-Palmer, P.; Mutjé, P. Mechanical and Micromechanical Tensile Strength of Eucalyptus Bleached Fibers Reinforced Polyoxymethylene Composites. *Composites, Part B* **2017**, *116*, 333−339.
(51) Khanlou, H. M.; Woodfield, P.; Summerscales, J.; Francucci, G.; King, B.; Talebian, S.; Foroughi, J.; Hall, W. Estimation of Mechanical Property Degradation of Poly(lactic acid) and Flax Fibre Reinforced Poly(lactic acid) Bio-composites during Thermal Processing. *Measurement* **2018**, *116*, 367−372.

https://doi.org/10.1021/acsami.3c00408
ACS Appl. Mater. Interfaces 2023, 15, 12443−12452